ULTRASONIC 3-D RECONSTRUCTION OF INCLUSIONS IN SOLIDS USING THE INVERSE BORN ALGORITHM

D.K. Hsu*, James H. Rose, and D.O. Thompson

Ames Laboratory, USDOE
Iowa State University
Ames, Iowa 50011

I. INTRODUCTION

Considerable progress has been made in recent years in the development of signal processing algorithms for use in ultrasonic non-destructive evaluation which yield the size, shape, and orientation of a flaw. This kind of flaw information is necessary in order that failure predictions of materials and components can be made from non-destructive tests. The signal processing algorithms that have been developed for ultrasonics are based upon both direct and inverse approximate solutions to the elastic wave scattering problem, and cover various ranges of the parameter ka where $k = \frac{2\pi}{\lambda}$ is the wave number of the ultrasound and a is a flaw size dimension. In order to use these algorithms effectively in the determination of flaw parameters, it has been found necessary to obtain measurements of the flaw at several viewing angles. At this time, there is no ultrasonic transducer available which permits this to be done efficiently and conveniently in the long and intermediate wavelength end of the spectrum. This region has been shown

*Permanent address: Physics Department, Colorado State University, Fort Collins, CO 80523. This material is also based on work supported by the National Science Foundation under Grant No. SPI-8165038.

The Ames Laboratory is operated for the U.S. Department of Energy by Iowa State University under Contract No. W-7405-ENG-82. This work was supported by the Director of Energy Research, Office of Basic Energy Sciences.

to be quite rich in flaw information and is appropriate to ultrasonic NDE in many practical applications (e.g., thick wall sections). Thus, the ultimate purpose of this work is to develop a composite transducer which will satisfy this need and which will permit the efficient utilization of various signal processing algorithms that have been developed. The immediate purpose of this present article is to discuss various steps that have been taken in the preparation of the intermediate frequency data protocol which is essential to the design of the desired transducer.

The use of the inverse Born approximation (IBA) to characterize flaws in elastic media has recently been studied both experimentally and theoretically by several groups [1,2]. In its general form the IBA coherently sums the longitudinal to longitudinal (L→L) (or transverse to transverse) scattering amplitude for all angles of incidence. As noted by Rose et al. [3], ellipsoidally shaped flaws can be characterized by treating each scattering record independently. This algorithm (the one dimensional inverse Born approximation, 1-D IBA) uses the L→L scattering amplitude in a single direction as the input. Its output is an estimate of the distance from the center of the flaw to the front surface tangent plane. The 1-D IBA has been studied experimentally for the case of voids and less extensively for inclusions. In this paper we continue the experimental characterization of the 1-D IBA. Two particular features of the algorithm were chosen for study. First, we used the algorithm to size a set of several different types of inclusions. It will be shown from this study that the algorithm can size an inclusion accurately using pitch-catch as well as pulse-echo data. For some of the inclusions studied, characteristic reasonances occurred in the flaw's excitation spectrum. The effect of these reasonances on the inversion algorithm was studied.

The ability of the 1-D IBA to provide information on the flaw's shape and orientation was also studied. For this work, we concentrated on the class of inclusion shapes that can be reasonably approximated by an ellipsoid. These results are expected to be fairly general since a wide variety of flaw shapes may be approximated by ellipsoids of different aspect ratio. Using experimental results of the 1-D Born algorithm for a number of scattering directions we determined the size, shape and orientation of nonspherical inclusions in terms of the six parameters (three semiaxes and three Euler angles) of the equivalent ellipsoid using a nonlinear least squares fitting procedure. The effects upon the results of limited apertures and the number of observation directions within the aperture were also assessed. With this technique, we have successfully reconstructed an approximately prolate spheroidal inclusion imbedded in a plastic host, an oblate spheroidal void in titanium and an approximately prolate spheroidal inclusion located very near the planar surface of a sample.

II. EXPERIMENTAL TECHNIQUE

In order to make a systematic study of the quantitative characterization of inclusion flaws, it is desirable to have a set of samples containing inclusions of known size, shape, orientation and material property. We have developed a sample fabrication technique in which spherical and nonspherical inclusions of various size and material are imbedded in a thermoplastic host. Since these samples are transparent, they have the distinct advantage of allowing comparisons to be made between the ultrasonically reconstructed results and the direct optical measurements. This is particularly convenient for studying arbitrarily oriented nonspherical inclusions.

The starting material of the host is Buehler's TRANSOPTIC, a thermoplastic resin that cures under heat and pressure. The disk-shaped samples, 3.2 cm in diameter and approximately 1 cm in thickness, were formed by compression molding in a mounting press. Inclusion materials were tin-lead solder, stainless steel and tungsten carbide. The size of the inclusions ranged from 50 to 300 μm and the depth of the inclusion was usually a few millimeters. Figure 1(a) shows a microscope photograph of a stainless steel inclusion and Fig. 1(b) shows the finished samples. In addition to being transparent, these samples can be easily machined and are very inexpensive to produce. They provide the experimenter with the freedom of investigating a variety of flaw configurations.

The experiments were carried out in a circular immersion tank equipped with translational and rotational adjustments. Three transducers were positioned above the water tank, two of them mounted on goniometers, for pulse-echo and pitch-catch experiments at various angles. The transducer was driven by a Panametrics 5052 pulser-receiver to produce a broad-band ultrasonic pulse. The received signal was digitized in a Tektronix 7912 digitizer and the signal processing was done on a Tektronix 4052 desktop computer.

The implementation of the one-dimensional inverse Born approximation followed the procedure described in Ref. 2. The determination of the zero of time (equivalent to locating the center of the flaw) was realized by estimating the cross-sectional area of the flaw in the scattering direction; the zero of time was taken to be at the maximum cross-sectional area of the flaw. The effective radius was obtained by estimating the characteristic function (defined ideally as $\gamma(r) = 1$ inside the flaw and $\gamma(r) = 0$ outside) from the 1-D IBA as

$$\gamma(r) = \text{constant} \times \int_0^\infty A(k) \frac{\sin \kappa r}{\kappa r} \, dk \qquad (1)$$

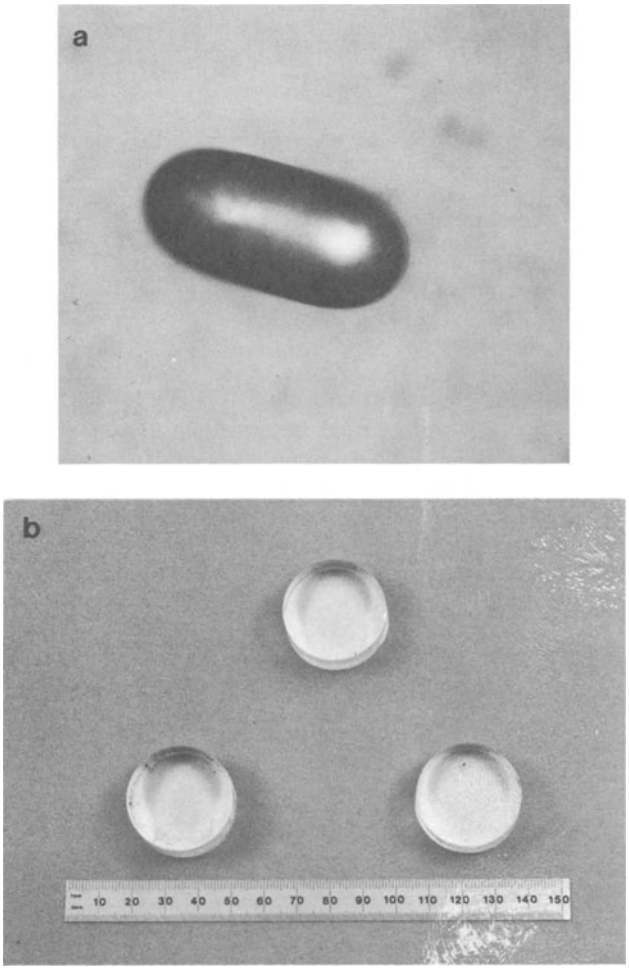

Fig. 1. (a) - Photograph of a 47 x 96 μm (semi-axes) stainless steel inclusion.
(b) - Plastic samples containing inclusions.

where κ is the wave number of the ultrasound, A(k) is the real part of the longitudinal (L→L) scattering amplitude and κ is the difference between the incident and the scattered wavevectors: $|\vec{\kappa}| = |\vec{k}_i - \vec{k}_s|$. For pulse-echo scattering κ is simply equal to 2k and for pitch-catch scattering κ is equal to $2k \cos \frac{\theta}{2}$, where θ is the angle between the transmitting and the receiving transducers, as shown in Fig. 2. The criterion used in estimating the effective radius was to take the value of r at one half the maximum value of the characteristic function.

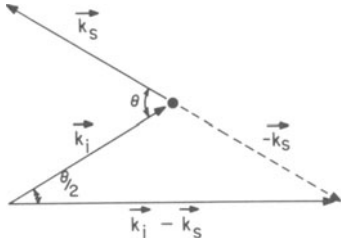

Fig. 2. Change in wavevector in pitch-catch scattering.

III. RESULTS ON SPHERICAL INCLUSIONS

A. Characteristic Resonance of Spherical Inclusions

In applying the one-dimensional inverse Born approximation to the sizing of included flaws, one is naturally concerned with possible characteristic resonances of the inclusion. Resonant oscillations occurring in the intermediate frequency range of $0.5<ka<2.5$ (where a is a characteristic dimension of the flaw) could cloud data interpretation and degrade the flaw sizing algorithm. Much is known about the resonant modes of spheres and other simple geometries from geophysical and underwater acoustics studies [4,5]. Although the size of the inclusions in NDE experiments is much smaller, the same

physical principles apply in terms of the dimensionless parameter ka. One therefore needs to address the question of what characteristic resonances might occur for a given inclusion and how would these resonances affect the inverse Born algorithm and the sizing results.

For inclusions with a high degree of geometric symmetry imbedded in an elastic medium of substantially lower acoustic impedance, sharp resonances or ringing are expected. A tungsten carbide sphere imbedded in a thermoplastic host represents such a case where the acoustic impedance of the inclusion is 35 times greater than that of the host. Given the large impedance mismatch we expected that the normal modes of vibration would be closely related to those of a free standing tungsten carbide sphere in vacuum. Figure 3 shows the scattered signal from a 198 μm radius tungsten carbide sphere in plastic and its frequency spectrum. We have measured the angular dependence of the amplitude of the 8.9 MHz resonance and the results are shown in Fig. 4. The amplitude went through zero at $\theta = 55°$ and reappeared with the opposite phase. The angular dependence is in good agreement with the associated Legendre polynomial $P_2^\circ(\cos\theta) = \frac{1}{2}(3\cos^2\theta - 1)$ which goes through zero at $\theta = 55°$. This resonance was attributed to the oblate-prolate mode (S_{20}) in the mixed mode family [6]. Measurements made in a higher frequency range revealed additional resonances at 13, 16.7 and 19.7 MHz and these were attributed to the S_{30}, S_{40} and S_{50} modes, respectively. In Table I, we compared the $k_s a$ values of these resonances with the $k_s a$ values taken from the mode chart compiled by Fraser and LeCraw [7] for a free isotopic spherical resonator and obtained good agreement. (Here k_s is the wave vector of the shear wave in the inclusion and a is the radius of the sphere). Our experimental results were also in good agreement with acoustic reflection measurements made with a hydrophone on large tungsten carbide spheres suspended in water [5].

In the mixed mode family, the lowest frequency resonance, the S_{20} mode, of a free sphere occurs at $k_s a \cong 2.7$ and this value is essentially independent of the material properties (e.g., Poisson's ratio). Rewriting $k_s a = 2.7$ as $ka(V_\ell^h/V_s^i) = 2.7$ where V_ℓ^h is the longitudinal velocity in the host, V_s^i is the shear velocity in the inclusion and k is the longitudinal wave vector in the host, one can therefore see that the S_{20} mode of oscillation would occur at a ka value less than 2.7 if $V_\ell^h > V_s^i$ and at $ka > 2.7$ if $V_\ell^h < V_s^i$. Since $0.5 < ka < 2.5$ is usually taken to be the minimum frequency bandwidth requirement for the one-dimensional inverse Born algorithm, a resonance occurring at $ka < 2.7$ might degrade the inversion algorithm; however, the strength and sharpness of the resonance must also be taken into account in assessing its influence on the inverse Born algorithm. For the tungsten carbide sphere, the S_{20} resonance occurs at ka=4 and is not expected to interfere severely with the inverse Born algorithm. For a solder sphere in plastic, $V_\ell^h/V_s^i = 1.9$ and several resonances can be expected in the inverse Born bandwidth.

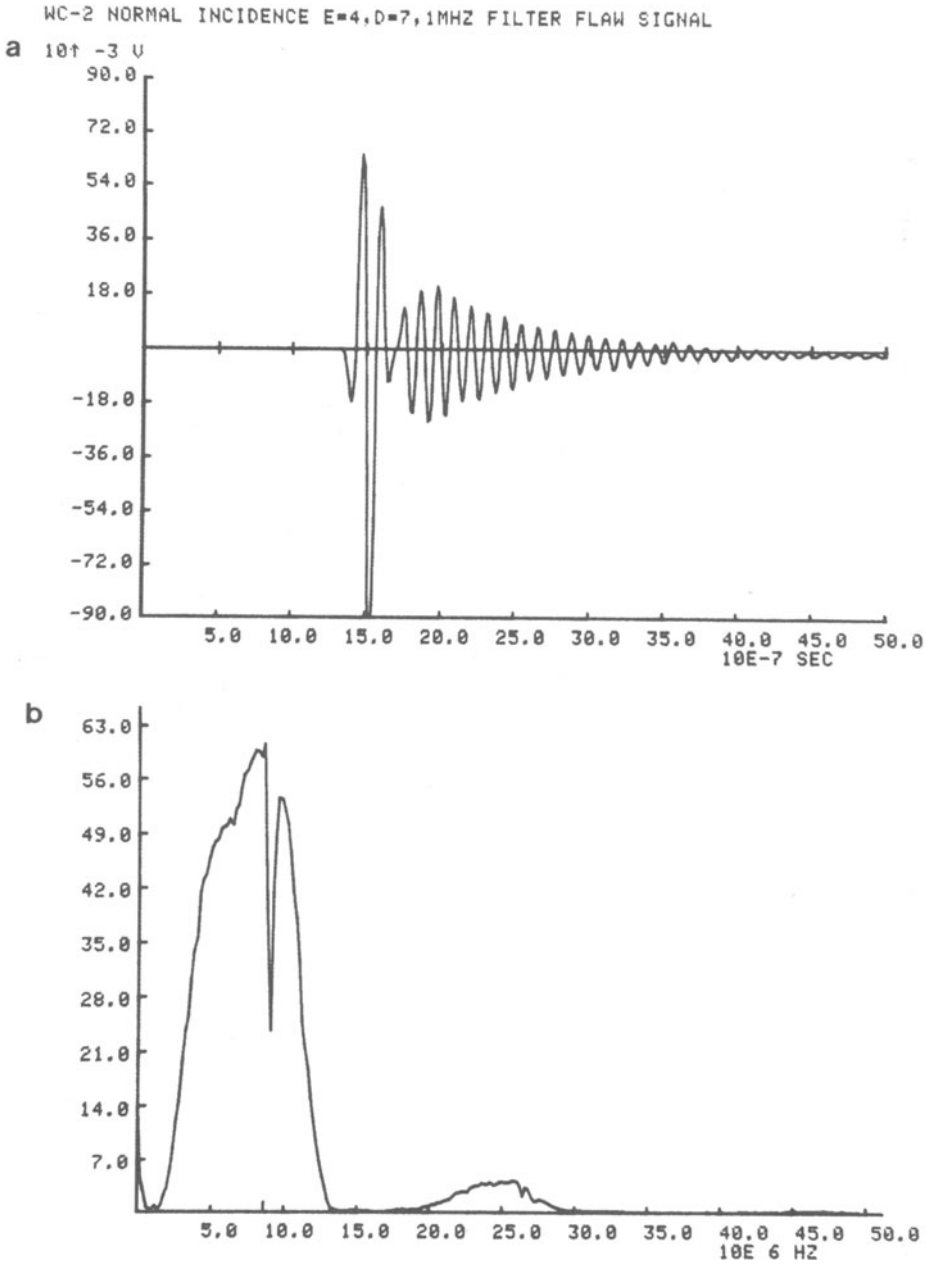

Fig. 3. (a) Time domain backscattering signal of a 198 μm radius tungsten carbide spherical inclusion.
(b) Fourier spectrum of the time domain signal in (a).

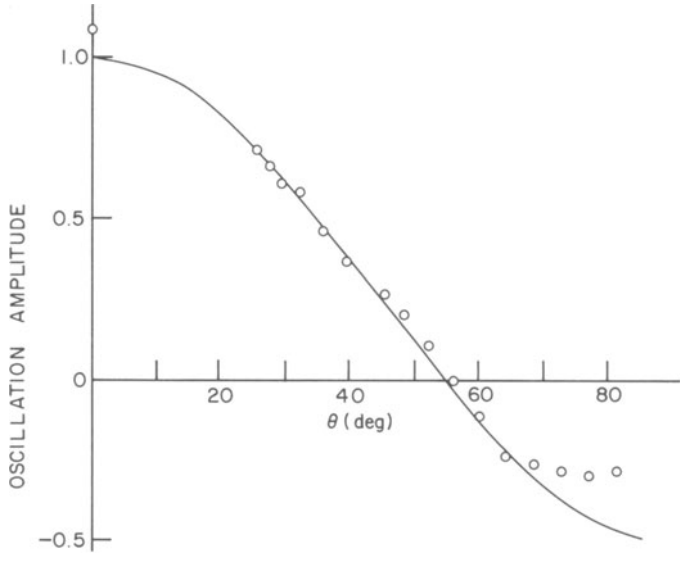

Fig. 4. Angular dependence of the amplitude of the trailing oscillations in Fig. 3(a). Here θ is the angle between the transmitting transducer and the receiving transducer. The solid line represents $(3\cos^2\theta-1)$.

Table I. Resonance modes of a tungsten carbide spherical inclusion.

Mode	f_{expt} (MHz)	$k_s a$ (expt)	$k_s a$ (mode chart)
S_{20}	8.9	2.6	2.68
S_{30}	13.0	3.8	3.91
S_{40}	16.7	4.9	5.01
S_{50}	~19.7	~5.7	6.06

NOTE: Shear velocity in tungsten carbide used in $k_s a$ was computed from manufacturer supplied data on Poisson ratio and Young's modulus.

In sizing the 198 μm radius tungsten carbide sphere, we used a 5 MHz (nominal center frequency) transducer and the resonance at 8.9 MHz was almost unobservable. Born inversion gave a radius estimate of approximately 170 μm. In this experiment some difficulties were encountered because of the "ring down" noise of the transducer below 2 MHz. Using a 10 MHz transducer, we also performed an inversion of the pitch-catch scattering data taken at $\theta=55°$ where the resonant oscillations vanish and obtained 188 μm as an estimate of the radius. Using this estimated radius and the mode chart value of $k_s a=2.68$, the shear velocity in tungsten carbide was deduced to be 3.9×10^5 cm/sec. This compared favorably with the handbook value of 3.98×10^5 cm/sec (or 4.3×10^5 cm/sec computed from manufacturer [8] supplied mechanical property data).

Experiments were performed to size a 114 μm solder sphere imbedded in plastic. Figure 5 shows the time domain and frequency domain scattering data. Born inversion gave a radius estimate of 92 μm. Although characteristic resonances occurred in the frequency range used in the Born inversion, the degradation did not appear to be serious. Qualitatively this could be explained by the fact that resonances of the solder sphere were not very strong or sharp.

B. Born Inversion of Pitch-Catch Scattering Data

As shown in Fig. 2, the change of wavevector for pitch-catch scattering is given by $2k \cos\frac{\theta}{2}$ where θ is the angle between the transmitting transducer and the receiving transducer. Equation (1) applies to pulse-echo scattering and pitch-catch scattering with κ set equal to $2k$ and $2k \cos\frac{\theta}{2}$, respectively. In the case of pitch-catch, the algorithm yields an estimate of the tangent plane distance in the $\vec{k}_i - \vec{k}_s$ direction. We applied the 1-D inverse Born algorithm to pitch-catch waveforms scattered from a 95 μm radius solder sphere imbedded in plastic and the results are shown in Fig. 6. For comparison the solid curve represents one-dimensional Born inversion results of theoretical scattering amplitudes of a 95 μm radius solder sphere in plastic. The theoretical scattering amplitudes were obtained via a numerical evaluation of the series solution of Ying and Truell [9]. In carrying out the 1-D Born inversion of the theoretical data, a bandwidth of $0.5<ka<2.2$ was used, in agreement with the experimental conditions. The agreement between the experiment and the theory was reasonably good.

IV. EQUIVALENT ELLIPSOID RECONSTRUCTION

In this section we describe a technique for determining the size, shape and orientation of an inclusion flaw in terms of an equivalent ellipsoid. The method begins with the tangent plane distances measured for a number of scattering directions confined within an experimentally accessible aperture and uses a nonlinear least squares fitting procedure to determine the three semiaxes (a_x, a_y, a_z) and the

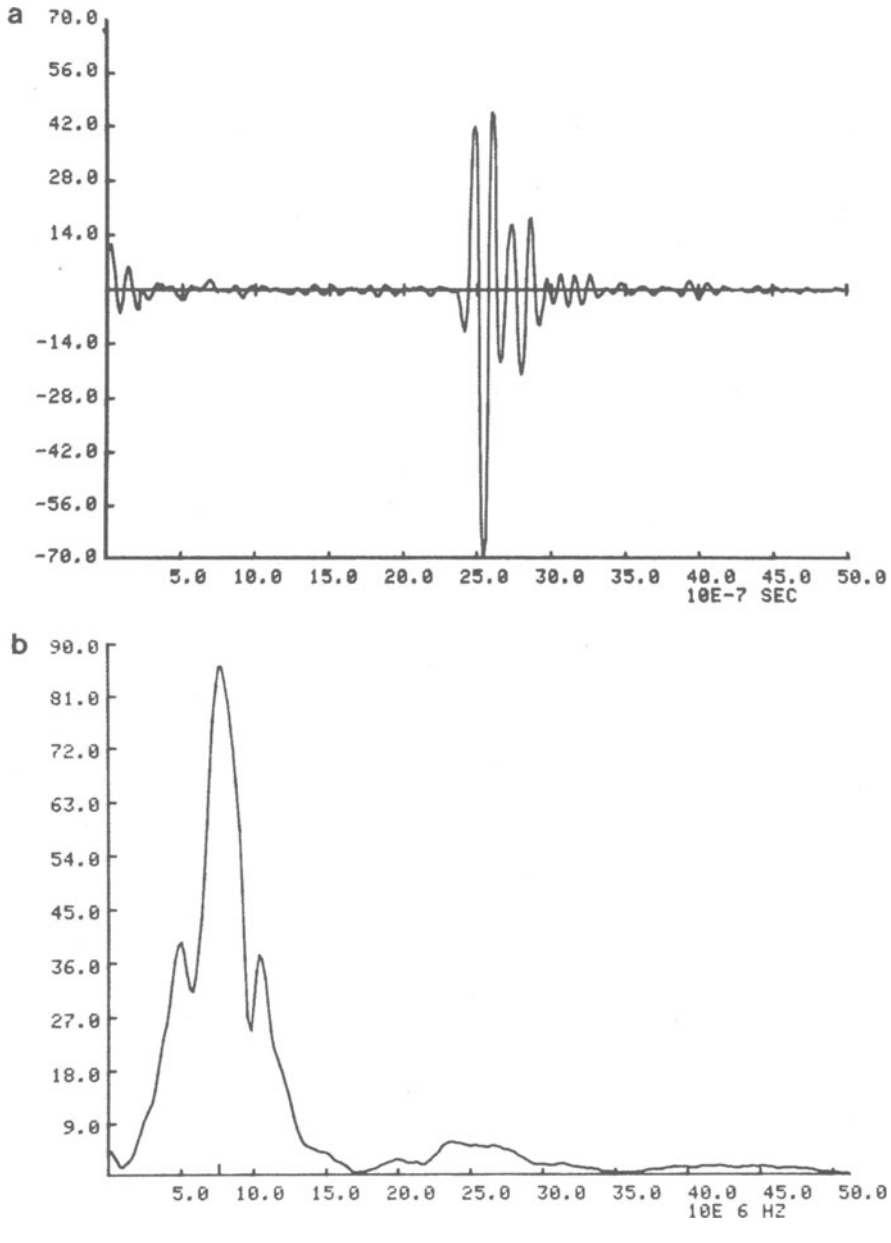

Fig. 5. (a) Backscattering signal of a 114 μm radius solder sphere inclusion.
(b) Fourier spectrum of the time domain signals in (a).

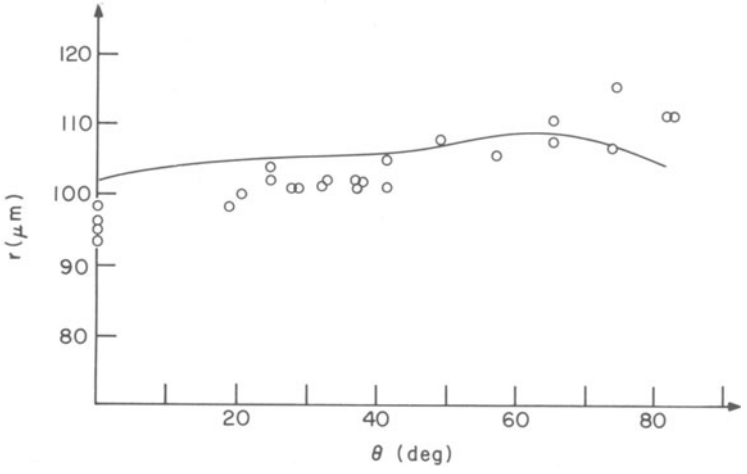

Fig. 6. Radius estimates by the one-dimensional Born inversion in the pitch-catch configuration for a 95 μm radius solder sphere inclusion. The dots are experimental results and the solid curve is obtained by inverting the exact theoretical scattering amplitude with a limited bandwidth.

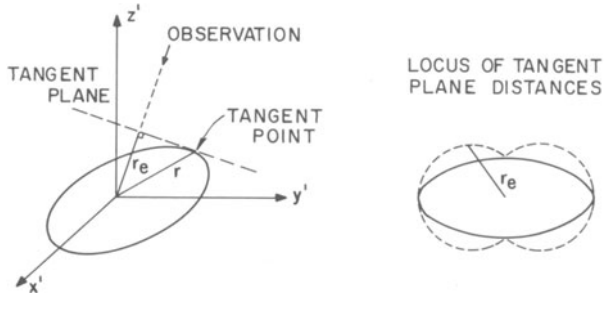

Fig. 7. Tangent plane distance (r_e) and tangent point distance (r).

three Euler angles of the equivalent ellipsoid [10] that fits the experimental results most closely and hopefully also represents a good approximation to the flaw.

For a given ellipsoid arbitrarily oriented in the laboratory system of coordinates (x',y',z'), its orientation can be specified in terms of three Euler angles ϕ, θ and ψ. Three successive rotations through the Euler angles in the sequence described in Ref. 11 bring the laboratory coordinates to coincide with the principal axes coordinates (x,y,z) of the ellipsoid. For a given observation direction specified by polar angle α' and azimuthal angle β', the tangent plane distance r_e is given by

$$r_e = (a_x^2 I^2 + a_y^2 J^2 + a_z^2 K^2)^{\frac{1}{2}} \tag{2}$$

where

$$I = a_{11} \sin\alpha'\cos\beta' + a_{12} \sin\alpha'\sin\beta' + a_{13}\cos\alpha'$$

$$J = a_{21} \sin\alpha'\cos\beta' + a_{22} \sin\alpha'\sin\beta' + a_{23} \cos\alpha'$$

$$K = a_{31} \sin\alpha'\cos\beta' + a_{32} \sin\alpha'\sin\beta' + a_{33} \cos\alpha'$$

and a_{ij} are elements of the coordinate rotation matrix in $\vec{x}=\vec{A}x'$. Each a_{ij} is a function of the three Euler angles ϕ, θ and ψ. The input data to the nonlinear least squares iteration routine therefore takes the form of (α',β',r_e) where r_e is the tangent plane distance obtained from the one-dimensional Born inversion for the observation direction specified by α' and β'. Based on Eq. (2), the iteration procedure determines the six parameters a_x, a_y, a_z, ϕ, θ and ψ of the ellipsoid that best fits the data in the least squares sense. We used a Marquardt's nonlinear least squares program in the Tektronix statistics package and performed the iteration on a Tektronix 4052 desktop computer. The iteration result contains tangent plane distances of the fitted ellipsoid for all directions and can be displayed together with the experimentally determined r_e for comparison.

Although the iteration result contains all the geometric information of the equivalent ellipsoid, it should be realized that, unless the scattering direction is along one of the principal axes, the tangent plane distance is generally different from the "tangent point distance" (i.e., the distance from the center to the point of contact with the incident wave front on the surface of the ellipsoid, denoted as r in Fig. 7). A three-dimensional display of r_e does <u>not</u> resemble the shape of an ellipsoid and it is therefore desirable to locate the tangent point on the surface for a given observation direction. In addition to yielding the true boundary of the ellipsoid, this step would also provide information about where and how much of the

surface is effectively "illuminated" by the incident waves in the observation aperture and thereby helps assessing the degree of confidence of the equivalent ellipsoid reconstruction. It can be shown that the coordinates of the tangent point in the laboratory frame are given by

$$x_o' = \frac{1}{r_e}\,(a_{11}\,a_x^2 I + a_{21}\,a_y^2 J + a_{31}\,a_z^2 K)$$

$$y_o' = \frac{1}{r_e}\,(a_{12}\,a_x^2 I + a_{22}\,a_y^2 J + a_{32}\,a_z^2 K) \qquad (3)$$

$$z_o' = \frac{1}{r_e}\,(a_{13}\,a_x^2 I + a_{23}\,a_y^2 J + a_{33}\,a_z^2 K)$$

The coordinates of the tangent point are functions of the six parameters resulted from the least squares iteration and the polar and azimuthal angles of the observation direction. It can further be shown that the "tangent point distance" r is given by

$$r = \frac{1}{r_e}\,(a_x^4 I^2 + a_y^4 J^2 + a_z^4 K^2)^{\frac{1}{2}} \qquad (4)$$

A display of r as a function of direction, together with the corresponding experimental points, will therefore serve as a visual realization of the size, shape and orientation of the flaw and graphically depicts the extension of flaw shape from the illuminated region to the "unseen" region.

VI. RESULTS OF ELLIPSOIDAL RECONSTRUCTION

To test the validity of the ellipsoidal reconstruction technique, we first applied it to the degenerate case of a spherical inclusion. Using Born inversion results of the 95 μm radius solder sphere (Fig. 6), the ellipsoidal reconstruction yielded good results: a_x = 91 μm, a_y = 89 μm and a_z = 95 μm. Experiments were then performed on an approximately prolate spheroidal inclusion (Fig. 1(a)) and the reconstruction was carried out for it. The utility of the method was next demonstrated in the reconstruction of an oblate spheroidal void in titanium. More recently, the technique has also been applied to reconstruct a near-surface prolate spheroidal inclusion in a study associated with testing the one-dimensional inverse Born algorithm for the sizing of near-surface flaws [12].

(1) Prolate spheroidal inclusion

A stainless steel inclusion with an approximate shape of a prolate spheroid (47 x 96 μm semiaxes, Fig. 1(a)) was imbedded in a plastic disk with its major axis tilted about 7° with respect to the parallel faces of the sample. Measurements were made at 25 scattering directions within a conical aperture of 39° half angle in the solid host. Tangent plane distances for various observation directions as obtained from the Born inversion are displayed in Fig. 8 where α' and β' are, respectively, the polar angle and the azimuthal angle of the observation direction in the laboratory system. Results of the ellipsoidal reconstruction are shown in Table II. It should be pointed out that, for small θ, equal and opposite values of ϕ and ψ correspond to compensating rotations about the z axis and are essentially equivalent to $\phi = 0$ and $\psi = 0$.

In the three-dimensional reconstruction of the flaw shape from a collection of one-dimensional inverse Born results at different observation directions, the effects of aperture size and number of observation directions are of interest. Using the data set shown in Fig. 8, we performed the ellipsoidal reconstruction with decreasing aperture size and number of data points. The results are also shown in Table II. It is undesirable to take data only at $\beta' = 0$, $\pi/2$, π, and $3\pi/2$ since this leads to nonuniqueness in the iterative fit

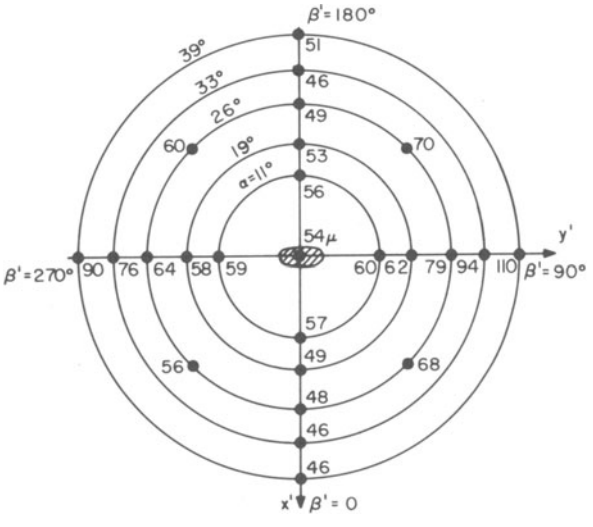

Fig. 8. Experimental results of the 47 x 96 μm (semiaxes) inclusion. The numbers beside the circles are the tangent plane distance (in μm), α' and β' are the polar angle and the azimuthal (in the solid) of the observation direction.

Table II. Results of the ellipsoidal reconstruction for the 47 x 96 μm (semi-axes) inclusion.

	Actual parameters	Ellipsoidal Reconstruction			
		A	B	C	D
a_x	47 μm	40	27	28	0
a_y	96	141	119	123	122
a_z	47	50	54	53	56
θ	~7°	14	8	9	2
ϕ	0	-71	-48	-47	7
ψ	0	69	47	46	8

A: 25 data points within a conical aperture of 39° half angle were used in the iteration.

B: 17 data points within a conical aperture of 26° half angle.

C: 9 data points, one at $\alpha' = 0$ and 8 at $\alpha' = 26°$.

D: 6 data points, one at $\alpha' = 0$, one at $\alpha' = 19°$ and 4 at $\alpha' = 11°$.

to the ellipsoid. The iteration scheme was found to be reasonably robust in terms of limited aperture and density of observation directions.

Figure 9 shows the tangent plane distance r_e as a function of the polar angle in the y'z' plane together with experimental points that fall on this plane. A similar plot for the x'z' plane is also shown in Fig. 9. Using Eq. (4) we further obtained the true representation of the ellipsoid surface in terms of the "tangent point distance" r. Figure 10 shows the y'z' cross-section of the reconstructed ellipsoid where the dots represent experimental points. As can be seen, the illuminated section of the surface covered by the tangent points subtends a much greater angular span than the 39° half angle aperture in the solid. A prolate spheroid with its major axis parallel to the sample surface therefore provides a high leverage for reconstruction. It should also be pointed out that the locus of the tangent points on the ellipsoid surface in general do not fall on a plane surface for interrogation directions confined to an arbitrary plane, they should therefore be displayed in a three-dimensional manner. In Fig. 10, however, the variation in x' is less than ± 4 μm and hence the figure represents a good approximation to a true y'z' cross-section of the ellipsoid.

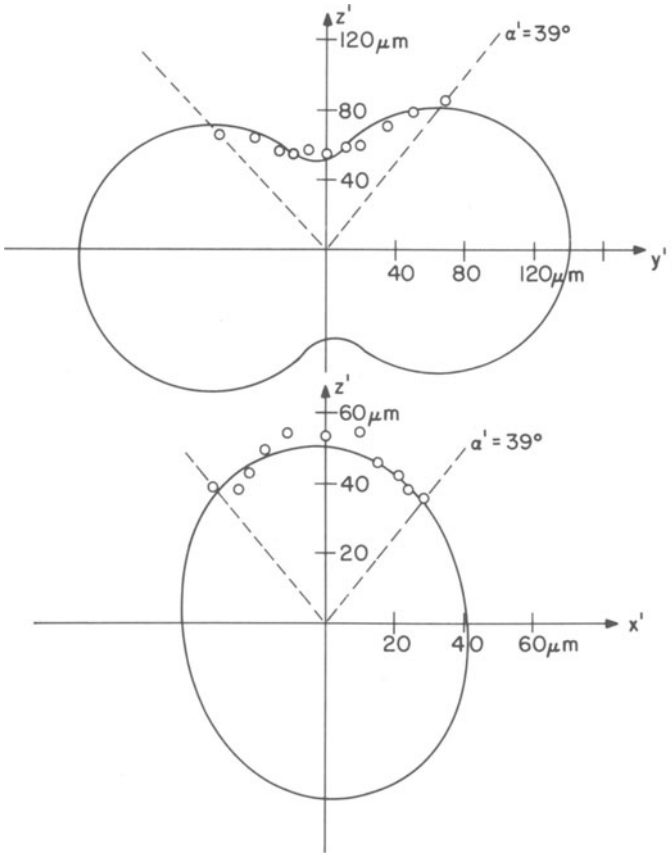

Fig. 9. The solid curves represent the tangent plane distance of the equivalent ellipsoid obtained by the least squares iteration based on the experimental data shown in Fig. 8 and the circles are experimental results. Both the y'z' and the x'z' cross-sections are shown here.

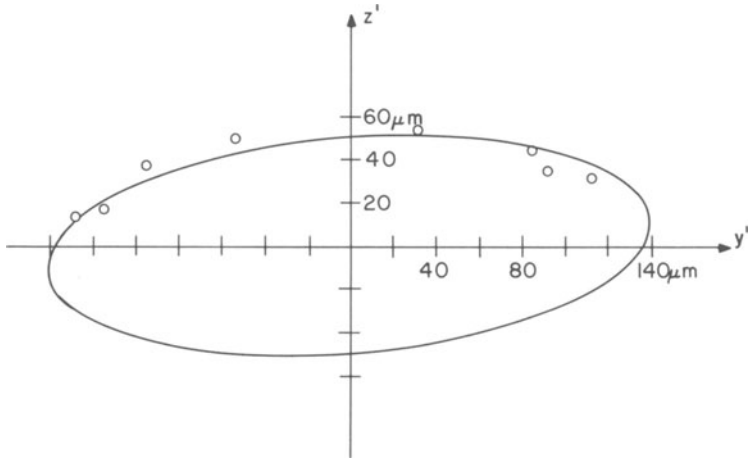

Fig. 10. y'z' cross-section of the equivalent ellipsoid for the 47 x 96 μm (semi-axes) inclusion after the $r_e \rightarrow r$ transformation. Experimental points lying in the y'z' plane are represented by open circles.

(2) Oblate spheroidal void in titanium

Although the results of the ellipsoidal reconstruction of the stainless steel inclusion in plastic are quite encouraging, it is necessary to demonstrate the validity of the technique for flaws in a realistic structural material. To this end we have carried out experiments on a 200 x 400 μm oblate spheroidal void in a diffusion-bonded titanium disk (provided by the DARPA/AFML program in quantitative non-destructive evaluation). Measurements were made for 21 observation directions in a conical aperture of 42° half angle in titanium (or 9° in water). Table III lists the inverse Born r_e values for these directions and Table IV shows the ellipsoid parameters obtained from the iteration based on the data in Table III. Figure 11 shows the y'z' cross-section of the reconstructed ellipsoid together with experimental points in the y'z' plane.

In the least squares fitting procedure, a set of "initial guess" values of the six parameters are needed to start the iteration. It was found that the results upon convergence were independent of the initial values and "wild guesses" led to identical results after a greater number of iterations. Table V shows two sets of initial guesses and their corresponding final results after the iteration converged. The interchange of a_x and a_y in the final results was

Table III. Tangent plane distance r_e of the 200 x 400 μm (semi-axes) oblate spheroidal void in titanium as obtained from 1-D Born inversion.

α' \ β'	0°	37°	90°	180°	217°	270°
13°	181 μm	228	186	178	176	194
22°	231	243	232	---	252	224
32°	275	---	291	---	286	285
42°	325	341	320	---	327	351

NOTE: Measurements were also made at $\alpha' = 0$ and repeated trials gave r_e = 201, 217, 201 and 176 μm.

Table IV. Results of ellipsoidal reconstruction of the 200 x 400 μm (semi-axes) oblate spheroidal void in titanium.

	Actual	Ellipsoid fit
a_x	400 μm	482 μm
a_y	400	397
a_z	200	179
θ	0°	-2°
ϕ	---	53
ψ	---	-176

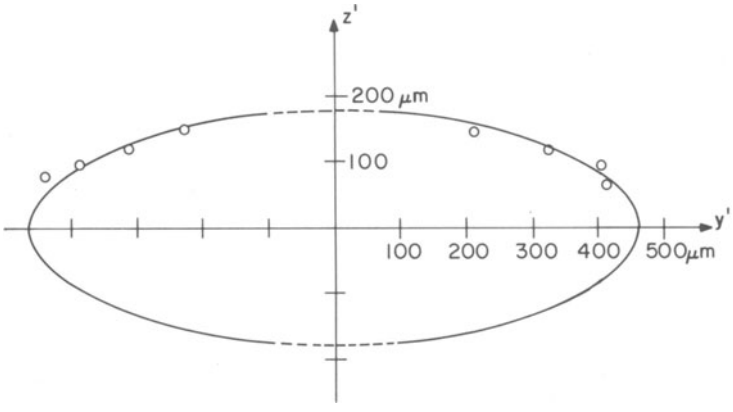

Fig. 11. Ellipsoidal reconstruction of the 200 x 400 μm (semiaxes) oblate spheroidal void in titanium. The ellipse represents the y'z' cross-section of the equivalent ellipsoid and the circles are experimental points confined in the y'z' plane.

caused by the 90° difference in the two sets of results and because θ is small the two sets of results are identical. Hence, although the reconstruction scheme is based on the assumption that the flaw can be reasonably approximated by an ellipsoid, no a priori knowledge about the order of magnitude of the parameters is required.

(3) Near-surface inclusion

The equivalent ellipsoid reconstruction scheme has recently been applied to the case of a near-surface inclusion. A 52 μm x 106 μm inclusion (approximately prolate spheroidal in shape) was located 220 μm below the flat surface of a sample and tilted 10° with respect to the flat surface of the sample. Pulse-echo measurements were made at oblique incidence with the polar angle in the 15°-54° range. Tangent plane distances were obtained for 40 observation directions using the one-dimensional Born inversion algorithm. Table VI shows the comparison between the actual values of the ellipsoid parameters and the iterated results. Here again the two angles ϕ and ψ are nearly equal and opposite and are physically equivalent to $\phi=\psi=0$ for small θ. A more complete account of this experiment is given in Ref. 12.

Table V. Iteration results from two different "initial guesses" for the 200 x 400 μm (semi-axes) oblate spheroidal void in titanium. Six data points were used, 5 at $\alpha' = 22°$ and one at $\alpha' = 0$.

	Initial	Converged	Initial	Converged
a_x	300 μm	436	1000 μm	310
a_y	400	310	500	436
a	200	199	10	199
θ	4°	5.7°	30°	5.7°
ϕ	305	47	170	47
ψ	24	-14	310	-104

Table VI. Ellipsoidal reconstruction results of the 52 x 106 μm (semi-axes) spheroidal inclusion.

Parameter	Actual values[1]	Iteration results
a_x	52 μm	57.5 μm
a_y	106 μm	120.3 μm
a_z	52 μm	42.1 μm
ϕ	0	-24.6°
θ	-10°	-7.0°
ψ	0	25.1°

1) from optical measurements.

Table VII. Ellipsoidal reconstruction of a flat circular crack using Opsal's theoretically calculated scattering amplitude.

	Ideal Result	Ellipsoidal Reconstruction		
		Face on, 51 points	edge on, Ω=60° 49 points	edge on, Ω=40° 25 points
a_x	1.0	1.052	1.002	0.995
a_y	1.0	1.052	1.002	0.995
a_z	0.16	0.16	0.131	0.371
θ	0°	0°	2.6°	1.7°

(4) Flat circular crack (theoretical data)

A flat circular crack may be regarded as an extreme case of an ellipsoidal void with $a_z=a_y$ and $a_z=0$. Theoretical calculation of the L→L scattering from a circular flat crack has been made by J. Opsal [13]. Figure 12 shows the tangent plane distances obtained from the one-dimensional Born inversion of the theoretical data (using the imaginary part of the scattering amplitude) [14] with a bandwidth of $k_{max}a = 10$. Using these theoretical values of tangent plane distances of a circular flat crack, we have tested the ellipsoidal reconstruction scheme in two ways. For a face-on observation configuration, we imposed a finite aperture of 50° half angle and assumed axial symmetry about the z axis. For an edge-on observation configuration, we imposed a "wedged pie section" aperture (also shown in Fig. 12). The results of the ellipsoidal iteration for both cases are summarized in Table VII.

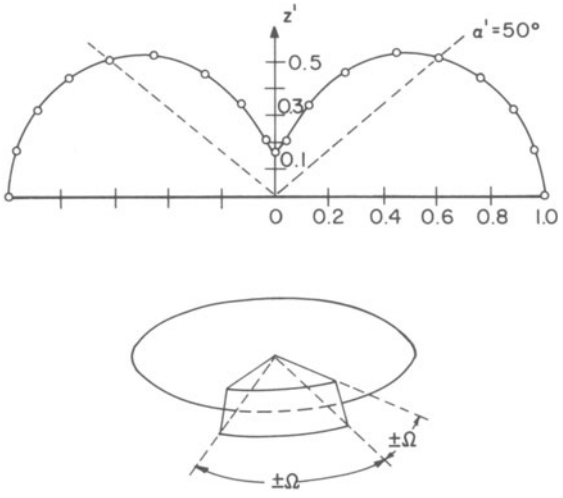

Fig. 12. Tangent plane distance as a function of polar angle α' obtained from band limited Born inversion of Opsal's theoretical data of a flat circular crack. Insert shows the "wedged pie section" aperture for the edge-on configuration discussed in the text.

VII. CONCLUSION

We have made an extensive study of the determination of geometric parameters (size, shape and orientation) of included flaws using the one-dimensional inverse Born approximation. Encouraging results were obtained even with a limited interrogation aperture. We have investigated the degradation of the 1-D Born inversion algorithm due to characteristic resonances of the inclusion flaw and due to surface-related scattering signals and found that, for the inclusions in our study, the degradation was not serious provided adequate frequency bandwidth was available. For inclusions in realistic structural materials, one would probably not expect high degrees of geometric symmetry in flaw shape and vast mismatch of impedance between the flaw and host material, strong and sharp characteristic resonances are therefore considered less likely.

In the course of developing a reconstruction scheme in terms of an equivalent ellipsoid, we have considered the general case of an arbitrarily oriented ellipsoidal flaw and analyzed in detail the tangent plane distance, the tangent point distance and the transformation between them. The method developed has performed quite well in determining the size, shape and orientation of ellipsoid-like flaws. We have demonstrated the reconstruction technique for an inclusion in the bulk, for a void in metal and for an inclusion near a fluid-solid interface.

In order to assess the degree of confidence of the flaw parameters obtained by the ellipsoidal reconstruction, a three-dimensional display of the reconstructed flaw together with the experimental data would be very useful. Such a display would serve as a visual realization of the goodness of the fit as well as the location and the extent of the illuminated area on the flaw surface. One can then judge the confidence of the reconstruction by studying the "extrapolation" from the illuminated area to the "unseen" portion of the surface. We are in the process of developing a three-dimensional display of our results. It is of future interest to investigate flaws with low leverage for reconstruction, i.e., flaws with very limited area of illumination by the available interrogation aperture. It would also be of interest to apply the ellipsoidal reconstruction technique to more extreme cases of ellipsoids such as penny-shaped and rod-like flaws when a wide frequency bandwidth becomes available for scattering experiments.

ACKNOWLEDGEMENTS

We would like to thank Dr. Jon Opsal for making the results of his calculations for flat cracks available to us in numerical form.

REFERENCES

1. R. C. Addison, R. K. Elsley and J. F. Martin, in Review of Progress in Quantitative NDE, Eds. D. O. Thompson and D. E. Chimenti, Pub. by Plenum Press 1, 251 (1981).
2. R. B. Thompson and T. A. Gray, in Review of Progress in Quantitative NDE, Eds. D. O. Thompson and D. E. Chimenti, Pub. by Plenum Press 1, 233 (1981).
3. J. H. Rose, R. K. Elsley, B. Tittmann, V. V. Varadan and V. K. Varadan, in Acoustic, Electromagnetic and Elastic Wave Scattering, Eds. V. V. Varadan and V. K. Varadan, Pergamon Press, pp. 605-614 (1980).
4. Y. Sato and Tatsuo Usami, Geophys. Mag. 31, 15 (1962).
5. W. G. Neubauer, R. H. Vogt, and L. R. Dragonette, J. Acoust. Soc. Am., 55, 1123 (1974), ibid 55, 1130 (1974).
6. B. A. Auld, Acoustic fields and waves in solids, see Vol. 2, 232-239 (1973) for a discussion of normal modes.
7. D. B. Fraser and R. C. LeCraw, Rev. Scientific Instrum., 35, 1113 (1964).
8. Industrial Tectronics, Inc., Ann Arbor, Michigan.
9. C. F. Ying and R. Truell, J. Appl. Phys. 27, 1086 (1955).
10. For a probabilistic inversion algorithm for crack-like flaws in terms of these parameters, see R. K. Elsley, in Review of Progress in Quantitative NDE, Eds. D. O. Thompson and D. E. Chimenti, Plenum Press 1 (1981).
11. H. Goldstein, Classical Mechanics, Addison Wesley, 1959, p. 107.
12. D. K. Hsu, J. H. Rose, R. B. Thompson and D. O. Thompson, submitted to Appl. Phys. Lett.
13. J. L. Opsal, in Proc. DARPA/AFML Review of Progress in Quantitative NDE, 292 (1980).
14. J. H. Rose, T. A. Gray, R. B. Thompson and J. L. Opsal, these proceedings.